



**HAL**  
open science

# CFD analysis of water vapor condensation in large containments: Numerical model, verification and validation

Ulrich Bieder, Axelle Herbette

► **To cite this version:**

Ulrich Bieder, Axelle Herbette. CFD analysis of water vapor condensation in large containments: Numerical model, verification and validation. Nuclear Engineering and Design, 2022, 395, pp.111861. 10.1016/j.nucengdes.2022.111861 . cea-04083173

**HAL Id: cea-04083173**

**<https://cea.hal.science/cea-04083173v1>**

Submitted on 22 Jul 2024

**HAL** is a multi-disciplinary open access archive for the deposit and dissemination of scientific research documents, whether they are published or not. The documents may come from teaching and research institutions in France or abroad, or from public or private research centers.

L'archive ouverte pluridisciplinaire **HAL**, est destinée au dépôt et à la diffusion de documents scientifiques de niveau recherche, publiés ou non, émanant des établissements d'enseignement et de recherche français ou étrangers, des laboratoires publics ou privés.

Copyright

# CFD Analysis of Water Vapor Condensation in large Containments: Numerical Model, Verification and Validation

*Ulrich Bieder, Axelle Herbette*

DES-STMF, CEA, Université Paris-Saclay

*F-91191 Gif-sur-Yvette, France*

*Ulrich.bieder@cea.fr :*

## ABSTRACT

In the event of a loss of coolant accident (LOCA) in a Pressurized Water Reactor (PWR), large quantities of water vapor and hydrogen might be released into the containment building. Increasing pressure and the risk of hydrogen deflagration can threaten the containment integrity. Water vapor condensation on cold containment structures modifies the pressure load on the containment structures. On the one hand, the total pressure reduces due to the decrease of the water vapor content of the containment atmosphere. On the other hand, the concentration of hydrogen increases, which can reach locally the threshold of deflagration or detonation. A Computational Fluid Dynamics (CFD) model is developed and tested in order to predict transients of the pressure and the concentrations of gaseous species in reactor containments after a LOCA. Since the free volume of the containment of typical French PWRs is between 50,000 m<sup>3</sup> and 80,000 m<sup>3</sup>, the CFD model requires significant simplifications.

The physical model and its simplifications as well the implementation in the CEA OpenSource CFD code *TrioCFD* are described. Model tests are presented in two steps. In a first step, verification tests are discussed to show that the condensation model is implemented correctly in the CFD code. In a second step, the model is validated against experimental data of the International Standard Problem ISP47. In this benchmark, steady state conditions between vapor injection and condensation were reached experimentally in the MISTRA test containment of the CEA. In phase A of the benchmark, an equilibrium was achieved between water vapor injection and water vapor condensation on temperature controlled cold walls. One incondensable gas, namely air, was present in the test vessel. In phase B, a second incondensable gas was added to the containment atmosphere, namely helium. Both steady state situations were analyzed with the CFD model. The calculations represent well the experiment when the predominant condensation paths are modelled. It is shown that the pressure in the containment vessel as well as the mean mass fractions of water vapor and air, as well as of helium in phase B, are calculated in accordance to the experiment. The temperature in the containment is overestimated. Measured vertical profiles of the species concentrations are reproduced correctly.

## 1. INTRODUCTION

Water vapor condensation is an important topic in nuclear engineering. The reactor accident of the year 2011 in Japan at Fukushima Daiichi demonstrated impressively the need to better understand flow and transport processes inside the containment building in order to design and evaluate efficient safety procedure. This accident was initiated by a tsunami due to an earthquake, followed by a station blackout. During such a severe accident in a nuclear power plant with a core degradation, large amount of water vapor is injected into the containment. Hydrogen is produced in the reactor core by the exothermic oxidation of Zircaloy by water vapor. As the accident progresses, water vapor condenses on the cold containment structures in the presence of air and hydrogen. This condensation process influences the pressure in the containment and the local concentration of hydrogen. Depending on the local concentrations of hydrogen, air and water vapor, after ignition, hydrogen can deflagrate or detonate (Yadav et al., 2016), putting at risk the integrity of the containment. Hence, vapor condensation plays an important role in the safety of nuclear power plants after severe accidents. According to Dehbi et al. (2013), such condensation processes with combined hydrogen release can also occur after loss of coolant accidents. Moreover, in-tube condensation can reduce the efficiency of passive containment coolers of advanced light water reactors due to the presence of incondensable gases. These gases can accumulate whereas the vapor concentration diminishes, which can lead to the presence of an added thermal resistance.

In order to assess containment codes for nuclear safety, the international standard problem ISP47 was organized (NEA/CSNI, 2007). One of the test facilities associated to ISP47 was the CEA facility MISTRA (Tkatschenko et al., 2005). The mixing of gases including the erosion of stratified layers by jets in the MISTRA facility was analyzed experimentally by Studer et al. (2012) and numerically by Ishay et al. (2015). Mixing of water vapor and air in the MISTRA facility in the presence of cold walls with steam condensation was subject of ISP47 (NEA/CSNI, 2007; Studer et al., 2007). Most of the analysis of the MISTRA ISP47 experiment has been performed with lumped parameter codes (e.g. Povilaiti, 2014). CFD scale calculations were often applied to analytical experiments (e.g. Bucci et al., 2008; Dehbi et al., 2013). Punetha et al. (2017) extended the CFD approach from analytical experiments to the small scale TOSQAN facility at IRSN. Studer et al. (2019) give more information on further MISTRA experiments and present an overview on more CEA activities on experimental and numerical programs related to containment flows and risks related to containment failure.

Only little information is available on the use of CFD on larger containments as for instance the MISTRA containment with a volume of 97.6 m<sup>3</sup>. Recently, two containment CFD code developments were reported, which are based on OpenFoam. Kim et al. (2018) presented the hydrogen distribution in an OPR1000 containment. Unfortunately, no information on the solved equations and on code validation is given. Kelm et al. (2019) outlined the development and validation strategy of the CFD code containmentFOAM that is developed at Forschungszentrum Juelich. Wall condensation can be implemented as volume source term or via wall fluxes, Kelm et al (2019) have chosen the first method. ContainmentFOAM not only treats turbulent mixing and water vapor condensation, but also radiative heat exchange and aerosol transport. Kelm et al., 2019 highlight the status of the work, provide first validation results and open research issues. Besides wall condensation, containmentFOAM also takes into account all aspects of the physics of species transport and homogeneous condensation (Kelm et al. 2021).

Although some sophisticated CFD models for containment applications including vapor condensation on cold walls exist, the use of simplified models that focus on the dominant physical processes will be, in the coming years, the preferable approach to analyze the flow in very large volumes as realistic PWR containments, which can have a volume of up to 80,000 m<sup>3</sup>. This paper tries to do a step in this direction. As a matter of course, significant model simplifications are necessary to treat real reactor containments as for instance the use of wall laws and the focus on the predominant transport phenomena. In the work presented here, a basic CFD model is described that has been developed at CEA to treat turbulent mixing of ideal gases in nuclear containments including the condensation of water vapor on cold walls. The numerical model and the made simplifications are described in detail. To verify the model and the coding, first fundamental separate effect tests were presented. Then to validate the application of the model to realistic nuclear containment conditions, the MISTRA ISP47 experiment is analyzed. The authors expect that this model can be used in the future to analyze the flow in PWR containments with a volume of up to 80,000 m<sup>3</sup>.

## 2. THE NUMERICAL MODEL

### 2.1 Water Vapor Condensation

Gaseous water diluted in air is called *steam* or *water vapor*. The word *steam* is typically used in common language to refer to the small water droplets that condense from hot water vapor, making cloud-like particles. In this article, the word

*water vapor* is used to better refer to the gaseous state of water that is mixed at low concentration with an incondensable gas of high concentration, air. Condensation occurs when the vapor is cooled below saturation temperature. Heterogeneous condensation is the non-equilibrium vapor-to-liquid phase transition in the presence of foreign objects. This phase transition comes along with a large variation in enthalpy. In this study, only heterogeneous condensation on cold surfaces is addressed. Homogeneous condensation is not taken into account. In the early phase of wall condensation, nucleation in the form of droplets occur on roughness elements of the wall. If the surface is hydrophilic, the droplets combine and form a liquid film. Then, condensation takes place on the liquid-vapor interface, on which a gas diffusion layer develops. Film formation is a widely used modeling hypothesis (Dehbi et al. 2013, Ambrosini et al. 2008) although a continuous film on cooled surfaces is not that easy to reach in technically relevant conditions and a film on containment structures is not granted.

The presence of incondensable gases have a great influence on energy and mass transfers at the liquid-vapor interface. Fig 1 presents a sketch of the liquid film and the diffusion boundary layer on a vertical plate. In the model, the film is not treated explicitly and it is assumed that the wall and the gas-liquid interface of the film have the same temperature, namely saturation temperature  $T_{sat}$ . Further, when condensation takes place, the partial pressure of vapor at the gas-liquid interface corresponds to saturation pressure  $P_{sat}$ .

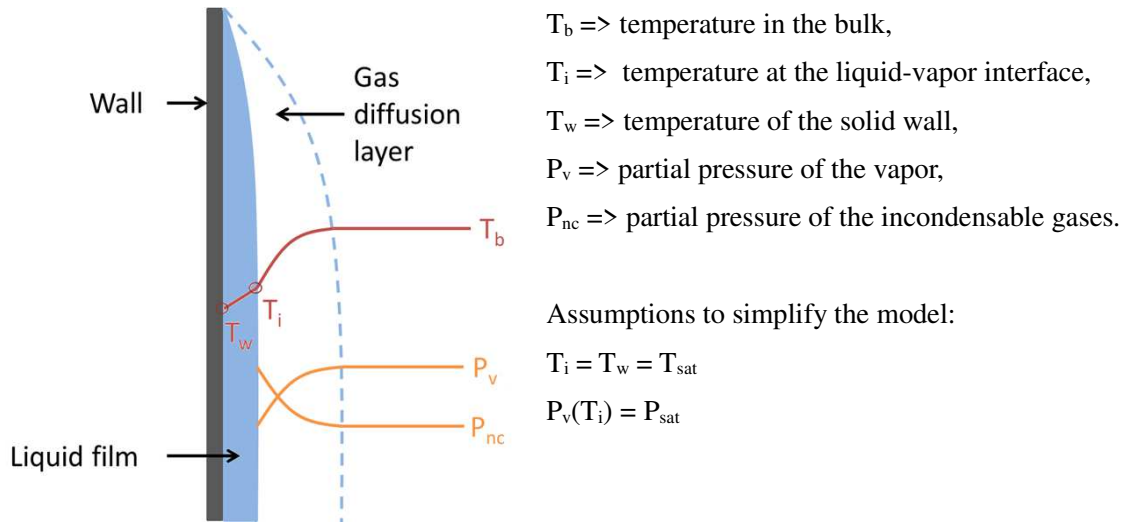


Fig. 1. Sketch of a liquid film on a wall and the associated profiles of temperature and partial pressures

When vapor condenses on a wall, the incondensable gases are driven by the flow to the interface where they accumulate. They build a barrier through which the vapor must diffuse to be able to condense on the liquid-vapor interface. In fact, when incondensable gases accumulate on the interface of the liquid film, their molar fractions become higher than in the bulk, producing a driving force for the diffusion of gases away from the interface. This diffusive flux is balanced by the mass flux to the interface due to condensation. Since total pressure remains constant, the pressure of vapor at the interface is lower than that in the bulk, creating a driving force for vapor diffusion.

According to Bird et al. (1963), the condensing mass flux of vapor on the wall  $m_v|_w$  (in  $\text{kg}/(\text{m}^2\text{s})$ ) in presence of incondensable gases can be calculated by the diffusion layer approach:

$$m_v|_w = \rho \frac{D+D_T}{\delta_d} \frac{y_{v,i} - y_{v,b}}{y_{nc,i}^{lm}} \cdot \frac{S}{V} \quad (1)$$

Here,  $\rho$  is the mixture density,  $y_v$  and  $y_{nc}$  are the mass fractions of vapor and incondensable gas with  $y_v + y_{nc} = 1$ .  $D$  and  $D_T$  are the molecular and turbulent mass diffusivities.  $\delta_d$  is a characteristic length of the boundary layer, which is calculated from wall functions depending on the distance of the unknown to the wall (see eq.(10)).  $y_{v,b}$  and  $y_{v,i}$  are the mass fractions of the vapor in the bulk and at the liquid-vapor interface that is at saturation temperature and pressure:  $y_{v,i} = M_v P_{sat} / (R T_{sat} \rho)$ .  $M_v$  is the molar weight of vapor and  $R$  the universal gas constant.  $y_{nc,i}^{lm}$  is a logarithmic mean concentration difference between interface and bulk,  $y_{nc,i}^{lm} = (y_{nc,i} - y_{nc,b}) / \ln(\frac{y_{nc,i}}{y_{nc,b}})$ , given by Bird et al. (1963).

The condensing mass flux is implemented as volume source term.  $S$  and  $V$  define the unit surface and volume. The condensing mass flux is acting on the control volume of the mesh-cell that is in contact to the wall with condensation.

## 2.2 Conservation equations

A mixture of water vapor (condensable gas) and air (incondensable gas) is considered. The fluid is Newtonian and is considered as a mixture of ideal gases. Density variations due to temperature and concentration variations are taken into account in the model. However, pressure variations due to compressibility are neglected, as they do not influence the flow in containments. Thus, a low Mach number model (Mach number  $Ma = \text{velocity/speed of sound}$ ) for dilatable gases is applied that has been developed at CEA particularly for natural convection flows (Elmo and Cioni, 2003; Saikali et al., 2019). According to the experience of the authors, this model outperforms models based on the SIMPLER family for natural convection flow. The total pressure  $P$  is separated in the thermodynamic pressure  $P_{th}$  that depends only on time  $t$  and the hydrodynamic pressure  $P_h$  that depends on both time and position  $x_i$ .  $P_h$  is very small compared to  $P_{th}$ .

$$P(t, x_i) = P_{th}(t) + P_h(t, x_i) \quad (2)$$

Turbulence is considered by Reynolds Averaged Navier Stokes equations (RANS). Thus, in the following, velocity  $u$ , temperature  $T$  and mass fraction  $y$  are Reynolds averaged quantities. The water vapor mass flux of wall condensation  $m_v|_w$  is taken into account as source terms in the conservation equation of the mass as well as in the conservation equations of energy and of each specie. The source terms are applied only on the near wall cells that are in contact to walls with condensation. The used conservation equations are summarized in the equations eq.(3) to eq.(7). Additionally, the equation of state of a binary ideal gas is given in eq.(8). The origin of the conservation equations of momentum, energy and species transport for a binary mixture are discussed in more detail in Annex I, II and III. The momentum transport due to the condensation on the wall ( $u_i m_v|_w$ ) as well as the enthalpy transport along species gradients ( $-\sum_{k=1}^N \rho D_k h_k \partial w_j / x_j$ ) are neglected at this state of modelling.

### Conservation of the total mass:

$$\rho \frac{\partial \rho}{\partial t} + \frac{\partial(\rho u_j)}{\partial x_j} = -m_v|_w \quad (3)$$

### Conservation of momentum (Navier-Stokes equations):

$$\rho \frac{\partial u_i}{\partial t} + \rho u_j \frac{\partial(u_i)}{\partial x_j} = -\frac{\partial P_h}{\partial x_i} + \frac{\partial}{\partial x_j} \left[ (\mu + \mu_T) \left( \frac{\partial u_i}{\partial x_j} + \frac{\partial u_j}{\partial x_i} \right) \right] + \rho g_i \quad (4)$$

The term  $-\frac{2}{3}(\mu + \mu_T) \delta_{ij} \text{div}(u_j)$  of the Reynolds stress tensor is not explicitly taken into account in the model. In the context of the expected thermal hydraulic conditions, this missing term modifies negligibly the hydraulic pressure  $P_h$ .

### Conservation of energy:

$$\rho c_p \frac{\partial T}{\partial t} + \rho c_p u_j \frac{\partial T}{\partial x_j} = \frac{\partial}{\partial x_j} \left[ (\lambda + \lambda_T) \frac{\partial T}{\partial x_j} \right] + c_{p,v} T m_v|_w + \frac{dP_{th}}{dt} \quad (5)$$

### Conservation of water vapor:

$$\rho \frac{\partial y_v}{\partial t} + \rho u_j \frac{\partial y_v}{\partial x_j} = \frac{\partial}{\partial x_j} \left[ (D + D_T) \frac{\partial y_v}{\partial x_j} \right] + m_v|_w \cdot (y_v - 1) \quad (6)$$

### Conservation of one incondensable gas:

$$\rho \frac{\partial y_{nc}}{\partial t} + \rho u_j \frac{\partial y_{nc}}{\partial x_j} = \frac{\partial}{\partial x_j} \left[ (D + D_T) \frac{\partial y_{nc}}{\partial x_j} \right] + m_v|_w \cdot y_{nc} \quad (7)$$

### Equation of state of a binary mixture of ideal gases:

$$\rho = \frac{P_{th}}{RT} \left( \frac{y_v}{M_v} + \frac{y_{nc}}{M_{nc}} \right)^{-1} \quad (8)$$

The transport equations of vapor (eq.(6)) and of all incondensable trace gases (eq.(7)) are taken into account in the model. The restriction that  $y_v + \sum y_{nc,i} = 1$  is used here to measure the error of the conservation of the mass of species. Such mass errors have been detected for high condensation rates and/or chemical reactions with very different reaction rates (system of stiff ordinary differential equations). Not solving all species transport equations can hide such mass conservation problems.

The turbulent viscosity  $\mu_T$ , the turbulent conductivity  $\lambda_T$  as well as the turbulent diffusivity  $D_T$  are calculated with the high Reynolds number k- $\epsilon$  model and turbulent Prandtl and Schmidt numbers, respectively, by assuming the similarity of moment, heat and species transfer. The physical properties of pure species are assumed constant. The physical properties of

the mixing are calculated from linear mixing laws. The near wall turbulent quantities are not affected by the condensation of water vapor. Reichardt's general wall function is used to calculate the momentum transfer across the boundary layer as well as for the prediction of  $k$  and  $\epsilon$  on the wall. Reichardt's law spans with one correlation viscous-, buffer- and turbulent sub-layer (Reichardt, 1951):

$$u^+ = \frac{1}{\kappa} \ln(1 + \kappa y^+) + 7.8 \left[ 1 - e^{\left(-\frac{y^+}{11}\right)} - \frac{y^+}{11} e^{\left(-\frac{y^+}{3}\right)} \right]. \quad (9)$$

Bieder et al. (2021) described the implementation of the wall law. Heat transfer is calculated with a Kader type wall function (Kader 1991):

$$q_w = \lambda \frac{T_f - T_w}{d} \quad \text{with} \quad d = T^+ \frac{\lambda}{\rho \cdot c_p \cdot u_\tau} \quad (10)$$

$$T^+ = Pr \cdot y^+ \cdot e^{-\Gamma} + (2.12 \cdot \ln(1 + y^+)) e^{-1/\Gamma} \quad \text{with} \quad \Gamma = \frac{0.01(Pr \cdot y^+)^4}{1 + 5 \cdot Pr^3 \cdot y^+} \quad (11)$$

Mass transfer is calculated analogously by using a constant Schmidt number  $Sc$ .

Using the equation of state of ideal gases for water vapor is not the best choice for conditions close to saturation. Far from saturation, the ideal gas assumption is acceptable for most gases including water vapor. As this assumption simplifies enormously the model and the coding (see also Kelm et al (2019)), the equation of state of ideal gases is used in the model. Applying of a more appropriate equation of state is planned for the future.

A crucial point for the quality of the calculation is the correct determination of the temporal variation of the thermodynamic pressure  $dP_{th}/dt$  that is dependent on the boundary conditions. *TrioCFD* considers two cases:

- For an open calculation domain with imposed pressure at a boundary,  $P_{th}$  is constant.
- For a closed calculation domain,  $P_{th}$  is calculated from a balance of the molar inventory of the calculation domain in the time interval  $dt$ . This balance includes the number of moles in the domain at instant  $t$  ( $N_n$ ), the number of moles at instant  $t+dt$  ( $N_{t+1}$ ) as well as the molar flows  $f_{bords}$  and  $f_{cond}$ , which are injected into the domain and which condense on domain walls:

$$N_{n+1} - N_n = (f_{bords} + f_{cond}) \cdot dt. \quad (9)$$

The implementation of this balance is discussed in more detail in section 2.3.

### 2.3 Implementation of the conservation equations

The conservation equations were discretized using a finite volume method on staggered grids. *TrioCFD* supports structured meshes on parallelepipeds and unstructured meshes on tetrahedrons. For structured meshes, the classical MAC spatial discretization method of Harlow and Welsh (1978) is applied (abbreviation VDF) and for unstructured meshes, a finite element based finite volume method is used (abbreviation VEF), which is an extension of the classical finite element of Crouzieux-Raviart (Angeli et al., 2018). For the VDF method, scalar unknowns such as pressure, temperature and mass fraction are located at the center of the elements, whereas the velocity components are taken normal to the faces of the elements. For the VEF method, vector- and scalar unknowns are located on element's faces and the pressure is located at the center and the vertices of an element. Both discretization methods are shown for the 2D case in Fig.2.

The VDF method is a well-established, highly performant CFD method that serves to create reference solutions in right-angled geometries, whereas the VEF method serves for realistic, industrial or near-industrial studies. The advantage of staggered mesh arrangement is the absence of spurious pressure modes (so-called checkers board modes), which are present in co-localized arrangement of velocity and pressure. FLUENT uses a similar nodalization for flows that demand a strong velocity-pressure coupling and to better handle non-linear source terms. According to the ANSYS-FLUENT documentation (FLUENT, 2009), the PRESTO (PREssure STaggering Option) scheme uses the discrete continuity balance for a staggered control volume about the face to compute the staggered (i.e., face) pressure. This procedure is similar in spirit to the staggered-grid schemes used with structured meshes (Patankar, 1980).

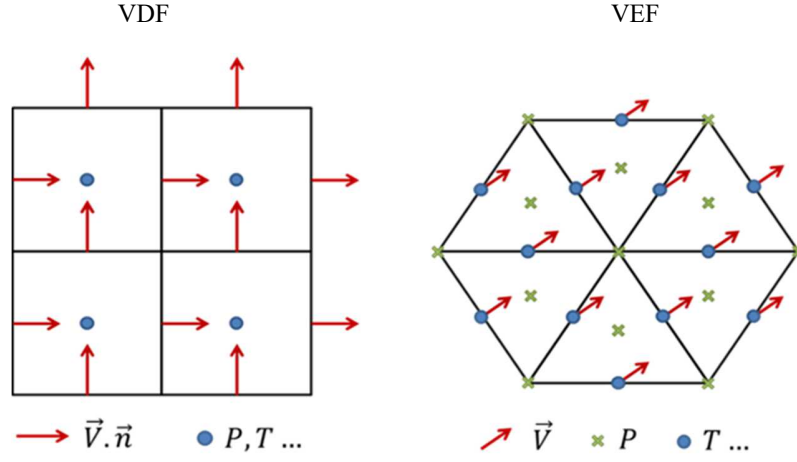


Fig. 2. Schematic representation of the VDF (left side) and the VEF discretization methods

For both discretization methods, the diffusion term is discretized by a 2<sup>nd</sup> order centered scheme. For time integration, the 1<sup>st</sup> order Euler explicit scheme is used. The time steps always respect the Courant-Friedrichs-Levy stability criteria (CFL) with  $CFL < 0.9$ . The momentum conservation equations are solved following the SOLA pressure projection method of Hirt et al. (1972). The resulting Poisson equation for the hydraulic pressure  $P_h$  is solved with a direct Cholesky method from the Petsc libraries. In order to avoid numerical instabilities in regions of high velocity gradients, the 2<sup>nd</sup> order muscl convection scheme with minmod limiter is applied for VEF (Ducros et al., 2010) and 3<sup>rd</sup> order schemes from the quick family are used for VDF.

The variation of the thermodynamic pressure is calculated from the mole balance eq.(9). For an ideal gas, the number of moles present in the calculation domain at instant  $n+1$  and  $n$  can be calculated according to:

$$N_{n+1} = \frac{P_{th,n+1}}{R} \sum_{i=1}^k \frac{V_i}{T_{i,n+1}} = \frac{P_{th,n+1}}{R} c_{n+1} \quad \text{with} \quad c_{n+1} = \sum_{i=1}^k \frac{V_i}{T_{i,n+1}}. \quad (10)$$

$V_i$  and  $T_i$  are volume and temperature of cell number  $i$ , and  $k$  is the total number of meshes of the domain. Analogously can be written:

$$N_n = \frac{P_{th,n}}{R} c_n \quad (11)$$

For an imposed velocity, the molar flow over  $l$  Dirichlet boundaries,  $f_{bords}$ , is calculated from:

$$f_{bords} = \frac{P_{th,n+1}}{R} \sum_{j=1}^l \sum_{i=1}^m \frac{S_i * u_{i,n+1}}{T_{i,n+1}} = \frac{P_{th,n+1}}{R} c_m, \quad \text{with} \quad c_m = \sum_{j=1}^l \sum_{i=1}^m \frac{S_i * u_{i,n+1}}{T_{i,n+1}} \quad (12)$$

$S_i$  is the surface of the boundary of cell  $i$ , and  $m$  is the number of cells of boundary  $j$ . The molar flow of condensing vapor,  $f_{cond}$ , is calculated from eq.(1) according to:  $f_{cond} = (\sum_{j=1}^m m_{v,j}/V_j)/M_v$ , with  $M_v$  the molar mass of water. Introducing these expressions in Eq.(9) leads to :

$$\frac{P_{th,n+1}}{R} c_{n+1} - \frac{P_{th,n}}{R} c_n = \left( \frac{P_{th,n+1}}{R} c_m + \frac{\dot{m}_v}{M_v} \right) * dt, \quad (13)$$

and finally to eq.(14) to predict the thermodynamic pressure at the instant  $n+1$ :

$$P_{th,n+1} = \frac{P_{th,n} c_n + R \frac{\dot{m}_v}{M_v} dt}{c_{n+1} - c_m dt} \quad (14)$$

### 3. VERIFICATION OF THE MODEL

The first step in the procedure to validate a numerical model is to assure that the model equations are implemented correctly. This step is called the verification step. As in the aimed application, besides wall condensation, natural and mixed convection are the main flow phenomena, only related test cases are discussed here.

#### 3.1 Mixing of two constituents in a closed cavity

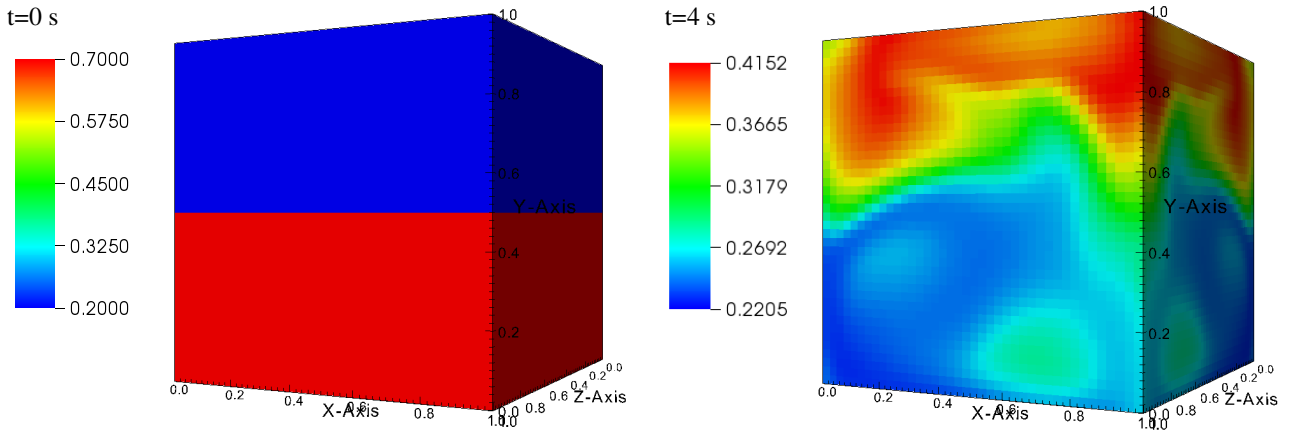
The objective of this test is to verify the mass balance when two fictive gaseous species of very different molar weights ( $M_1=0.01 \text{ kg/mol}$ ;  $M_2=10 \text{ kg/mol}$ ) are mixed in a closed cavity. Initially, gas is at rest, atmospheric pressure and temperature ( $P_0 = 101.325 \text{ kPa}$  and  $T_0=363 \text{ K}$ ). The two species are present in a closed, cubic cavity of  $1 \text{ m}^3$  with adiabatic, impermeable walls. The mass fractions in the upper half of the cavity are  $y_{u,1} = 0.2$  and  $y_{u,2} = 0.8$  and in the lower half  $y_{l,1} = 0.7$  and  $y_{l,2} = 0.3$ . As the gas mixture in the upper half of the cavity is heavier than in the lower half, the gases start mixing due to buoyancy forces. This mixing process is illustrated in Fig.3 (VDF calculation), where the mass fraction of the light gas (component 1) is shown for the cavity walls at  $t = 0 \text{ s}$ ,  $4 \text{ s}$  and  $8 \text{ s}$ . The temporal course of the mass fractions in one point in the center of the cavity is added to the figure. Only the first 10 seconds of the mixing process are shown.

After a period of convection driven mixing of about 5 seconds, diffusion becomes the driving mixing process. After about 100 seconds, the two species become perfectly mixed. The analytical solution in the final state of component 1 is calculated from a simple mass balance according to:

$$y_1 = \left( 1 + \frac{y_{u,2} \left( \frac{y_{l,1}}{M_1} + \frac{y_{l,2}}{M_2} \right) + y_{l,2} \left( \frac{y_{u,1}}{M_1} + \frac{y_{u,2}}{M_2} \right)}{y_{u,1} \left( \frac{y_{l,1}}{M_1} + \frac{y_{l,2}}{M_2} \right) + y_{l,1} \left( \frac{y_{u,1}}{M_1} + \frac{y_{u,2}}{M_2} \right)} \right)^{-1} \quad \text{and} \quad (15a)$$

$$y_2 = 1 - y_1 \quad (15b)$$

The resulting mass fractions of the two completely mixed species are  $y_1 = 0.311$  and  $y_2 = 0.689$ . Both discretization methods, VDF and VEF, calculate these concentrations correctly. Total pressure and temperature do not vary during the transient.



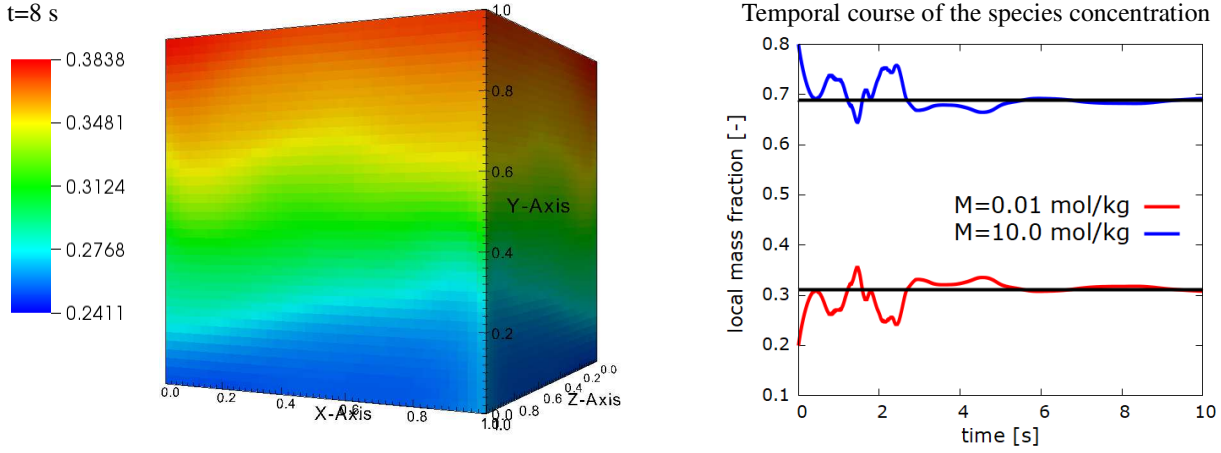


Fig. 3. Dynamic of the mixing in a closed cavity is shown by the mass fraction of the light gas; heavy gas on top and light gas on bottom. Black lines represent theoretical steady state values (eq.(15a) and eq.(15b))

### 3.2 Condensation in a closed cavity.

The objective of this test is to verify the mass balance when water vapor condenses in a closed cavity. The cavity of volume  $V=1 \text{ m}^3$  at atmospheric pressure and saturation temperature ( $P_0 = 101.325 \text{ kPa}$  and  $T_0 = 363 \text{ K}$ ) is filled initially with a mixture of air ( $M_{nc} = 0.029 \text{ kg/mol}$ ,  $y_{nc,0} = 0.42$ ) and vapor ( $M_v=0.018 \text{ kg/mol}$ ,  $y_{v,0}=0.58$ ). The cubic geometry of the calculation domain is shown in Fig.3. All walls of the cavity are impermeable to the constituents. The cold wall at  $x = 0 \text{ m}$  is maintained at a constant temperature of  $T_c = 303 \text{ K}$ ; the hot wall at  $x = 1 \text{ m}$  is maintained at  $T_h = 363 \text{ K}$ . All other walls are adiabatic.

A natural convection flow establishes in the cavity due to density differences, which are driven by the oppositely located hot and cold walls and, as long as condensation takes place, by species concentration differences. The temporal development of condensation mass flow, volume-averaged mass fraction, thermodynamic pressure and volume-averaged temperature are shown in Fig. 4a to Fig.4d. Analytical solutions are estimated for the final state based on the Boussinesq approximation. In the final state, the mean temperature should attain approximately

$$T_{ss} = (T_c + T_h)/2 = 333 \text{ K}. \quad (16)$$

In the final state, all available vapor in the cavity has condensed on the cold wall. Since the cold wall is at saturation temperature, the partial pressure of vapor in the cavity corresponds to the saturation pressure at  $T_c = 303 \text{ K}$ , i.e.  $P_v = 4.2 \text{ kPa}$ . This partial pressure corresponds to a final mass of water vapor in the cavity of:

$$m_{v,ss} = M_v \frac{P_v V}{RT_{ss}} = 0.027 \text{ kg}.$$

The mass of the air is not changing during the condensation process:

$$m_{nc,ss} = m_{nc,0} = \frac{y_{nc,0} P_0 V}{\frac{y_{nc,0} M_{nc} + y_{v,0} M_v}{RT_0}} = 0.302 \text{ kg}.$$

This mass of air leads at the end of the condensation process to a mass fraction of the incondensable gas of:

$$y_{nc,ss} = \frac{m_{nc,ss}}{m_{v,ss} + m_{nc,ss}} = 0.92 \quad (17a)$$

and of water vapor of:

$$y_{v,ss} = 1 - y_{nc,ss} = 0.08. \quad (17b)$$

The thermodynamic pressure can be estimated to about:

$$P_{ss} = \left( \frac{m_{v,ss}}{M_v} + \frac{m_{nc,ss}}{M_{nc}} \right) \frac{RT_{ss}}{V} = 33 \text{ kPa} \quad (18)$$

In contrary to solutions based on the Boussinesq approximation, in dilatable modelling, the steady state fields of velocity, concentration and temperature are not point-symmetric to the cavity center. However, since constant physical properties are applied in this test, mean values close to those for incompressible fluids are expected in the cavity. Fig. 4 shows that these estimated conditions at steady state are achieved by the calculation (VEF discretization is shown). The same steady state conditions are achieved by the VDF discretization.

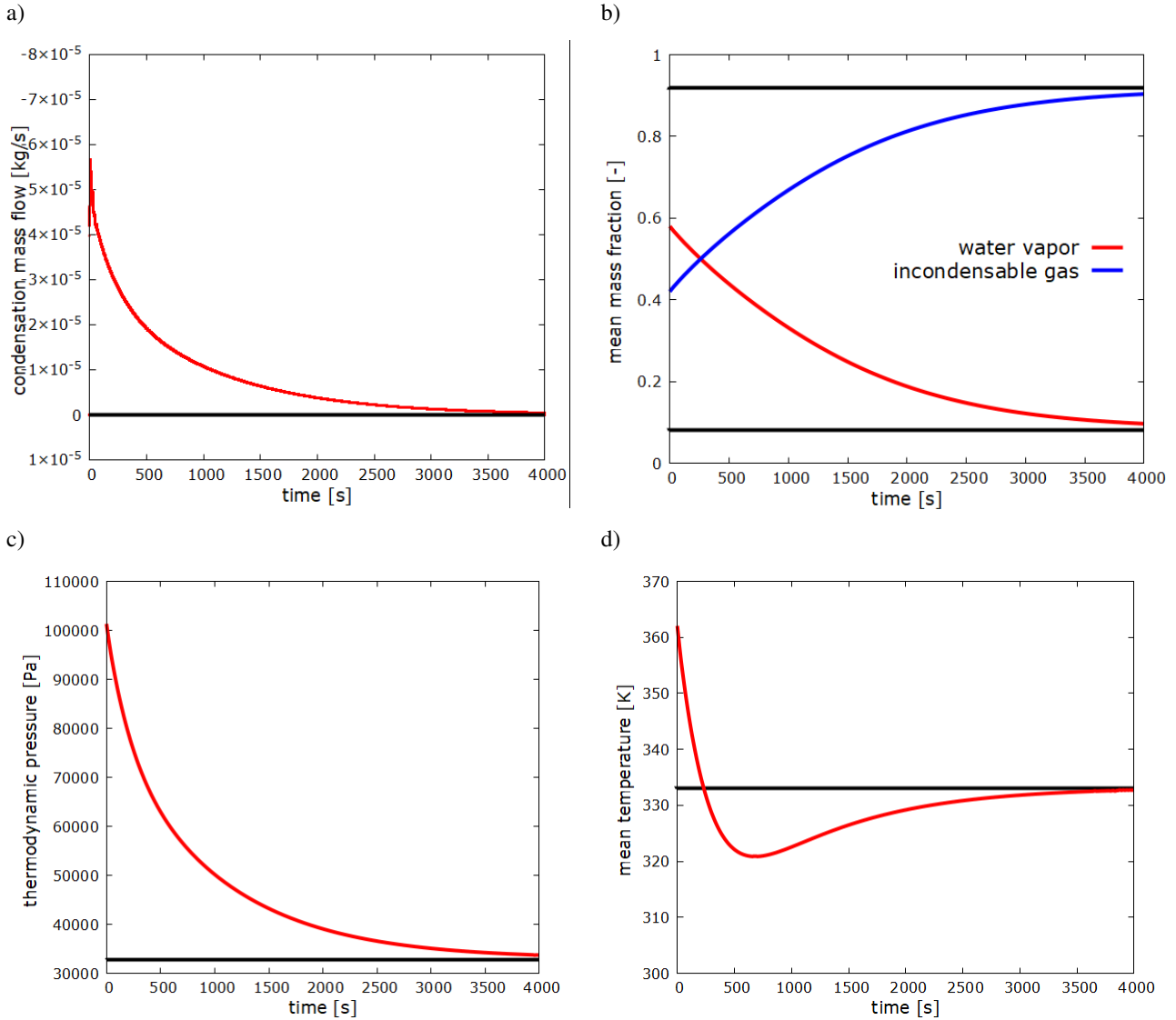


Fig. 4. Temporal course of condensation mass flow (a), mean species mass fraction (b), thermodynamic pressure (c) and mean temperature (d). Black lines represent estimated steady state values according to eq.(16), eqs.(17a, 17b) and eq.(18).

### 3.3 Condensation in an open cavity with vapor injection

The objective of this test is to verify the mass balance when water vapor condenses in a cavity with simultaneous vapor injection. The cubic cavity of  $1 \text{ m}^3$  at  $P_0 = 300 \text{ kPa}$  and  $389 \text{ K}$  is filled initially close to saturation conditions with a mixture of air ( $M_{nc} = 0.029 \text{ kg/mol}$ ,  $y_{nc,0} = 0.436$ ) and water vapor ( $M_v = 0.018 \text{ kg/mol}$ ,  $y_{v,0} = 0.564$ ). The cold wall at  $x = 1 \text{ m}$  is maintained at a constant temperature of  $T_c = 388 \text{ K}$  (cavity see Fig.3). All other walls are adiabatic. Water vapor is injected at the constant temperature  $T_i = 472 \text{ K}$  and the mass flow rate  $0.01 \text{ kg/s}$  into the cavity via a  $0.1 \text{ m}$  long square inlet channel, which has a cross-section of  $0.01 \text{ m}^2$ . The channel is located in the center of the cavity's bottom wall.

A transient of about  $600 \text{ s}$  was calculated until an equilibrium establishes between water vapor injection and condensation. VDF results are shown in Fig.5. The spatial distribution of the main quantities in the cavity is given for the instant  $t = 300 \text{ s}$ . The vertical visualization-plane cuts the cavity and the injection channel in their mid-plane at  $y = 0.5 \text{ m}$ . The velocity vectors in the mid-plane are shown in Fig.5a, the magnitude of the velocity is added in color scale. The central jet and large circulation zones are visible. Temperature and vapor mass fraction are given in the color plots Fig.5b and Fig 5c, respectively. Non-symmetric spatial distributions of all quantities are readily visible as well as the formation of vapor and

temperature stratification. The cold wall at  $x = 1 \text{ m}$  (right wall), on which vapor condenses, acts as energy and vapor sink. Thus, the gas mixture becomes colder and air richer as the flow descends along this cold wall due its higher density. This mixture of high density accumulates in the lower part of the cavity. The resulting stratification of the density is well visible in Fig.5d. On the adiabatic wall at  $x = 0 \text{ m}$ , the flow cannot penetrate from above into the lower air-rich region of the cavity due to buoyancy forces (Fig.5a).

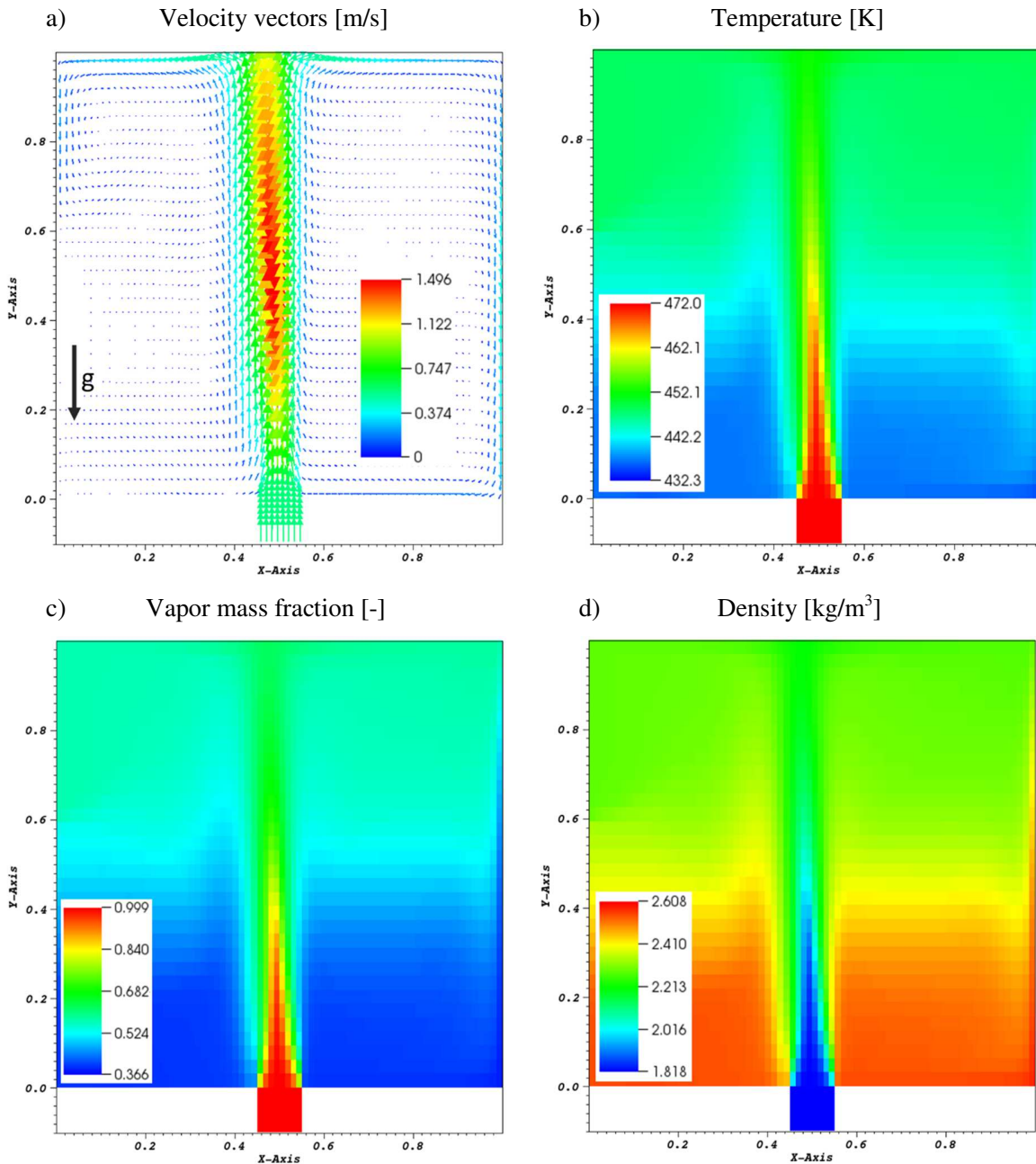


Fig. 5 Simultaneous water vapor injection and condensation in a cavity. Distribution in the cavity mid-plane of a) velocity vectors, b) temperature, c) vapor mass fraction and d) density.

Fig.6 shows the temporal course up to  $600 \text{ s}$  of the total condensation mass flow (Fig.6a) as well as the volume-averaged values of the mass fractions of water vapor and the incondensable gas air (Fig.6b). It is visible that the vapor condensation mass flow approaches the vapor injection flow and the mean mass fractions converge to constant values. Further, the

transients of the mean temperature (Fig.6d) and of the thermodynamic pressure (Fig.6c) are shown. After an increase of the mean temperature due to the hot injection and compression, the temperature is also approaching a constant value. At 600 s, the thermodynamic pressure reaches 396 kPa.

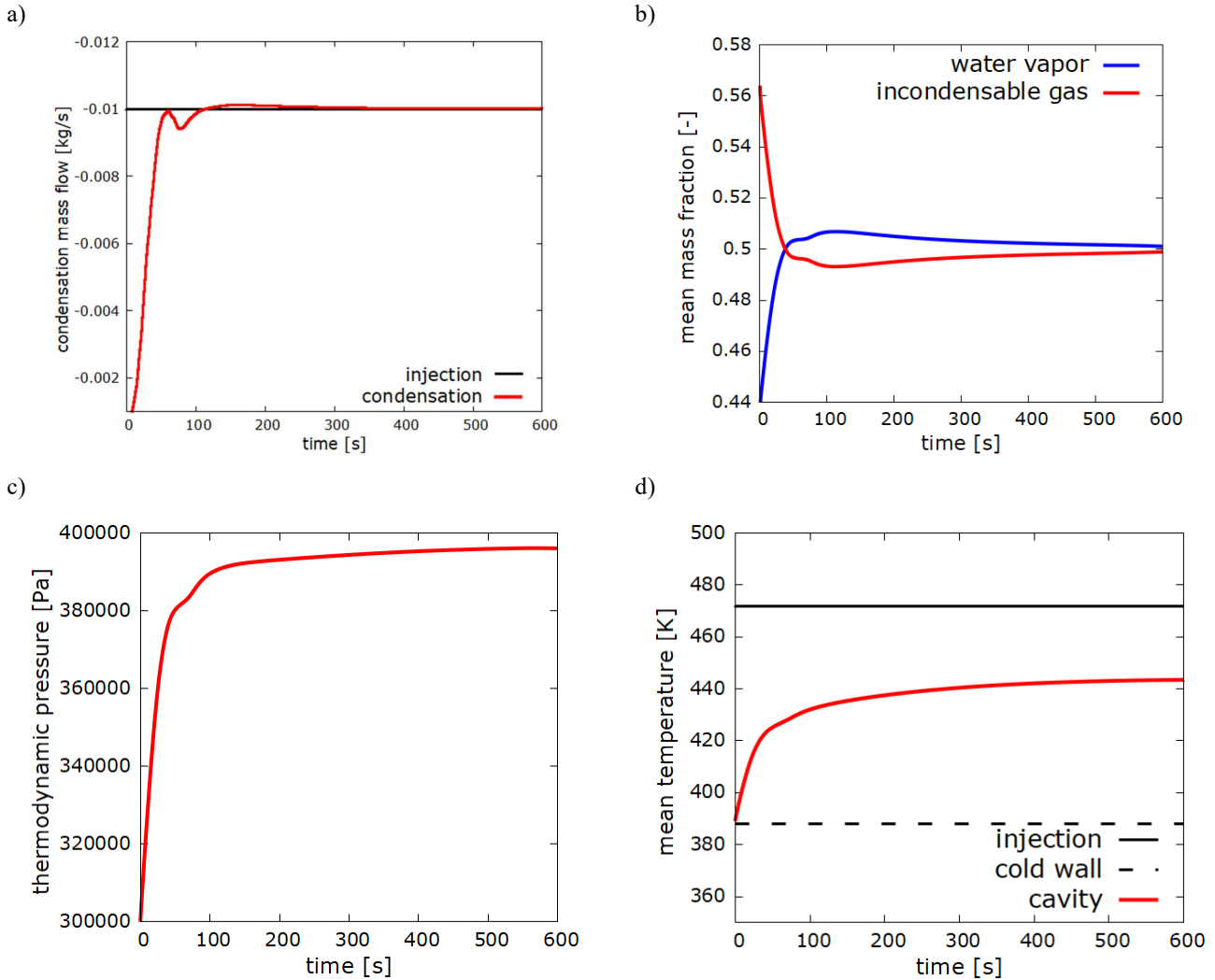


Fig. 6. Temporal course of total condensation mass flow as well as of volume averaged mean vapor mass fraction and temperature.

Analytical solutions for this test case do not exist. Pressure, temperature and vapor mass fraction within the cavity at steady state conditions are dependent on the flow dynamics and here especially on the characteristics of the boundary layers that develop on the cold wall. Hence, further model validation is required.

It is interesting to note that Kassem (2020) has analyzed with the same model mixed and forced convection experiments that have been made in the CONAN facility (Ambrosini et al.2008) of the University of Pisa, Italy. A good agreement to the channel-flow type wall condensation experiment was reached for locations where the boundary layers were fully developed (limitation related to the use of wall functions). The consistent implementation of the source terms was evaluated by assessing the correctness of mass balances of all species to assure the conservation of the mass of both condensable- and incondensable species. The energy balance of the channel flow was also evaluated successfully.

## 4. VALIDATION OF THE MODEL

The second step in the procedure to validate a numerical model is to assure that the model represents correctly the physics of the aimed application. This step is called the validation step. For this purpose, ISP47 MISTRA experiment was analyzed with the model that has been verified in section 3. For the modelling of the MISTRA experiment, Best Practice Guidelines of the *TrioCFD* code were followed.

### 4.1 The MISTRA test facility

The MISTRA facility (Studer et al., 2012 and Studer et al., 2019) is shown in Fig.7a. MISTRA consists of a cylindrical vessel, a flat cap and an elliptical bottom, which are joined by twin flanges. The vessel is made of stainless steel with an internal volume of  $97.6 \text{ m}^3$ . The height and inner diameter of the vessel are  $7.38 \text{ m}$  and  $4.25 \text{ m}$ , respectively. These dimensions correspond to a linear length scale ratio of  $0.1$  in relation to a typical French PWR containment. The outside of the vessel is insulated by  $0.2 \text{ m}$  of rock wool. Three condensers are inserted into the MISTRA vessel. Each condenser is an open cylinder with an inner diameter of  $3.82 \text{ m}$ . The condensers share the same vertical axis with the vessel walls and are located on top of each other. They are separated vertically by gaps of  $0.12 \text{ m}$ . The condensers have the following temperature controlled inner surface areas: bottom condenser  $26.2 \text{ m}^2$ , center - and top condenser  $21.4 \text{ m}^2$ . The outer surface of the condensers are adiabatic due to a  $0.02 \text{ m}$  isolation. The condensate is recovered in gutters, one gutter for each condenser. The facility contains measuring sensors for temperature (T) and helium concentration (C) as well as pressure sensors (P). Moreover, one spychole exists in the middle of the vessel for measuring a local velocity profile. The locations of these sensors and of the spychole are shown in Fig.7b. A diffusion cone is used for gas injection. This device is installed in the center axis near the bottom of the vessel (see Fig.7b). The cone has an outlet diameter of  $0.2 \text{ m}$ . A porous material within the cone assures a flat velocity profile at the outlet level. The flow rate is controlled by velocity measurements with sonic pipes.

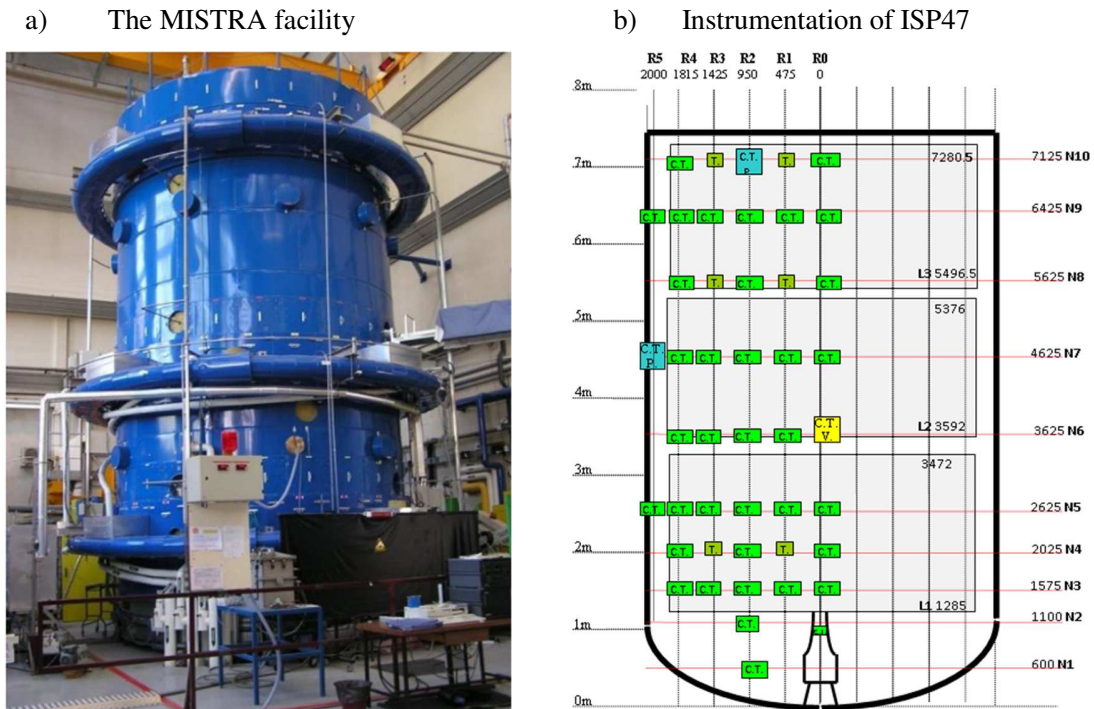


Fig. 7 The MISTRA facility at the assigned time of ISP 47; a) global view and b) instrumentation of ISP 47

The MISTRA test sequence of ISP47 was conducted in four successive phases (NEA CSNI, 2007; Vendel et al. 2002 ):

- **Preheating phase:** initially the test vessel is filled with pure air at ambient conditions. Condensers are preheated above saturation temperature and superheated steam is injected into the vessel to heat up the steel structures.
- **Phase A:** condensers are cooled below saturation temperature; a steady state is reached between injecting and condensing water vapor. One incondensable gas (air) is present in the containment vessel.

- Transient phase: for 1826 seconds, a helium mass flow of 0.01016 kg/s is added to the main water vapor injection.
- Phase B: after shut-off of the helium injection, a new steady state is reached between water vapor injection and vapor condensation in the presence of two incondensable gases (air and helium).

In the study presented here, the steady state situations of phase A and of phase B are analyzed.

#### 4.2 CAD model and Meshing

The CAD model was build with SALOME<sup>1</sup>. Due to the axis symmetrical geometry of the facility, only one half of the facility was modelled. Further simplification to 2D axis-symmetry was omitted as a 3D model should be validated. The CAD model is shown in Fig.8a, the flat cap and the symmetry plane are hidden for a better visualization. The CAD model was imported in *step* format into the commercial mesh generator ANSYS-ICEMCFD. In order to use the VEF discretization method of *TrioCFD*, a pure tetrahedral meshing was created. In a first step, a surface meshing with triangles was build. Then, in a second step, the volume was filled with tetrahedrons using the Delaunay method. Various meshes of different refinement were created for mesh sensitivity studies. Here only two meshes are discussed:

- Coarse mesh: The size of the tetrahedrons on all solid walls is twice as fine as the maximum size of the volume mesh in order to resolve boundary layers more precisely. Two layers of prismatic cells were introduced on the condenser walls. Each prism was divided into three tetrahedral elements. This coarse mesh has 510,000 tetrahedral cells, representing about 1 million control volumes for velocity, temperature and species since, in VEF, vectors and scalars are discretized in the center of the element's faces.
- Fine mesh: The reference size of the meshing was reduced by 30%. One layer of prismatic cells was introduced on the condenser and vessel walls. After splitting all elements into tetrahedrons, the fine mesh yields about 1,600,000 tetrahedral cells

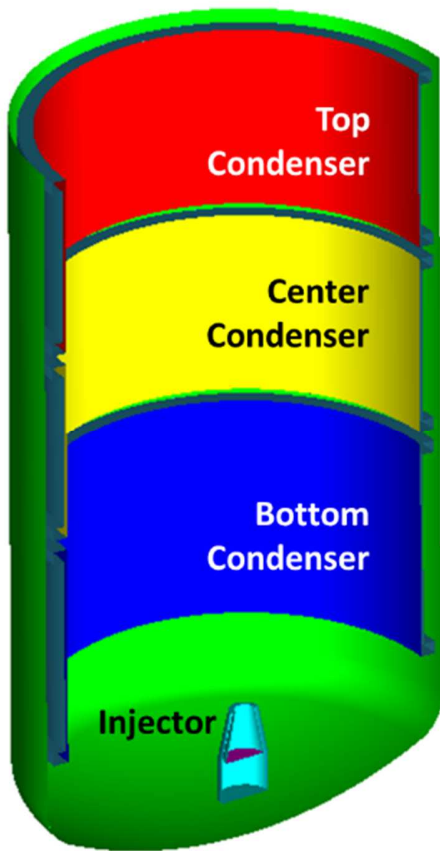
The particular treatment of the near wall mesh in the cases of coarse and fine mesh with two and one layer of prismatic cells, respectively, leads to similar  $y^+$  values on the condenser walls, i.e. to about  $y^+ \approx 40$ . An expansion factor of 2% was used for both meshes. This lead to a very smooth transition of the tetrahedron sizes from the near wall mesh to the mesh within the free volume.

The vertical cut through the fine mesh is give in Fig.8b. The mesh refinement near the condensers and the external wall is well visible. It is also visible that the meshing in the vapor injection nozzle seems being too coarse to simulate the injection of the central jet. Therefore, separate effect studies with the two mesh refinements in the nozzle were conducted. These tests showed an insensitivity of the two meshes in the injection nozzle on the overall jet formation. As the CFL is respected in the calculation, a finer meshing in the injection nozzle reduces the time step to calculation times that are prohibitive in the actual stage of the analysis. After all, the time step imposed by the CFL for the coarse mesh is about 0.004 s and that for the fine mesh is about 0.002 s.

---

<sup>1</sup> <https://salome-platform.org/>

a) CAD model build with SALOME



b) Fine meshing

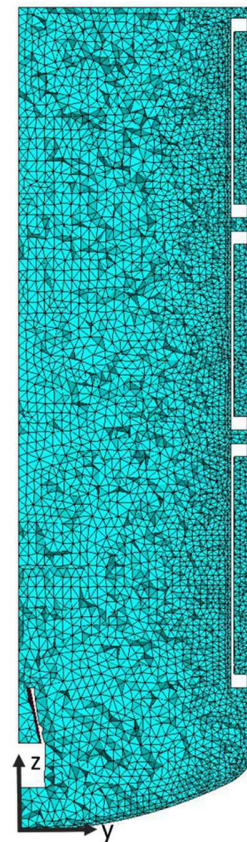


Fig. 8 The MISTRA facility; a) CAD model showing the injector as well as the top, center and bottom condenser, b) fine meshing in the central cut plane at  $y = 0\text{ m}$

It is important to note that a realistic  $80,000\text{ m}^3$  PWR containment can be simulated with about  $2.5 \times 10^9$  meshes by using the tetrahedron size of the fine mesh. Such large meshes are used at CEA on a regular basis for production calculations with *TrioCFD*.

### 4.3 Physical properties

Air and water vapor are assumed ideal gases. The physical properties of the binary air/vapor mixture and the ternary air/helium/vapor mixtures, respectively, were calculated by means of linear mixing rules from the properties of pure components. Dependencies of the properties on temperature and pressure are not taken into account. The physical properties of pure species air, helium and water vapor are given in Table 1 for  $471\text{ K}$  and  $101,325\text{ Pa}$ .

Table 1 Physical properties of air and water vapor

Gas	Dynamic viscosity [Pa s]	Isobaric heat capacity [J/kg/K]	Thermal conductivity [W/m/K]	Molar weight [mol/kg]
Air	$2.58 \times 10^{-5}$	1023	0.038	0.02897
Helium	$2.43 \times 10^{-5}$	5195	0.170	0.00400
Water vapor	$1.61 \times 10^{-5}$	1979	0.033	0.01801

The corresponding Prandtl numbers ( $Pr = (\mu \cdot c_p) / \lambda$ ) are approximately  $0.7$  for air,  $0.95$  for water vapor and  $0.7$  for helium. To estimate the mass diffusivity  $D$ , a constant Schmidt number ( $Sc = \mu / (\rho \cdot D)$ ) of  $Sc = 1$  is used. The turbulent Prandtl number is taken to  $0.7$  and the turbulent Schmidt number is taken to  $1.0$ .

#### 4.4 Initial and boundary conditions

Table 2 summarizes initial and boundary conditions for phase A and phase B of ISP47 that were taken from Studer et al. (2007). Averages over four experiments were calculated for steady state conditions at the end of the corresponding test phase. Studer et al. (2007) estimated the mentioned experimental uncertainties from the standard deviations of the four tests.

Table 2 Experimental initial and boundary conditions of ISP47

	Phase A	Phase B
Temperature bottom condenser [K]	388.15 ± 0.8	387.15 ± 0.8
Temperature center condenser [K]	387.85 ± 0.8	386.85 ± 0.8
Temperature top condenser [K]	388.25 ± 0.8	387.25 ± 0.8
Steam injection rate [g/s]	130.4 ± 0.1	130.4 ± 0.1
Temperature injected steam [K]	471.85 ± 0.5	471.85 ± 0.5
Initial pressure [Pa]	1.03 × 10 <sup>5</sup>	1.03 × 10 <sup>5</sup>
Initial temperature [K]	300.15	300.15
Initial mass air [kg]	117.5	117.51
Initial mass helium [kg]	0	18,55
Initial mass water vapor [kg]	0	0
Water vapor injection [kg/s]	0.0635	0.0635

Two hypotheses were tested to model heat losses to the environment and associated spurious condensation:

- Neumann boundary conditions with *adiabatic* vessel walls and
- Dirichlet boundary conditions with *imposed temperature* on the external vessel walls.

To use the second hypothesis, the experimentalists have derived the correlation eq.(19) that allows to account for spurious condensation of vapor that occurs on the internal vessel walls (40%), in the sump (40%) and on the isolated walls of the condensers (20%). The correlation was deduced from experimental data by using mass balance considerations (Studer, 2019). The wall temperature  $T_w$  is give in °C as a function of vessel height  $z$ , given in  $m$ :

$$T_w = 0.0325 \cdot z^4 - 0.5014 \cdot z^3 + 2.2819 \cdot z^2 - 1.6717 \cdot z + 116.35 . \quad (19)$$

Wall functions are used on all solid walls, that is Reichardt's law for momentum transport and transport of  $k$  and  $\epsilon$  as well as Kader type functions for heat- and trace gas transport. The authors are aware that the deformation of the boundary layers on the wall with condensing water vapor as described in Fig.1 cannot be simulated correctly with these wall laws. However, as long as wall resolved modelling, that would be the correct approach, is not practical in studies on containments of nuclear reactors with acceptable computation times, this drawback must be accepted. The walls are also considered as non-permeable for constituents. As only one half of the MISTRA vessel is modelled as shown in Fig.8, symmetry conditions are used for all conservation equations on the plane that closes the calculation domain in the vertical mid vessel center.

#### 4.5 Steady state solution of phase A

Two modelling hypothesis were tested in the analysis of phase A of ISP47 concerning mesh refinement and treatment of the heat losses to the environment. Three simulation models were defined and tested:

- The *basic model* is built on the coarse mesh. The vessel walls are assumed adiabatic,
- The *improved model* also uses the coarse mesh. The temperature of the external vessel wall follows the profile defined by eq.(19),
- The *fine model* is based on the fine mesh. The temperature of the external vessel wall follows the profile defined by eq.(19).

In the experiment, after the pre-heating phase, a long transient of about  $15,000 s$  was performed at constant vapor injection rate, starting at atmospheric pressure (Povilaitis et al., 2014). An equilibrium between injected and condensed water vapor will be achieved at the end of the transient as discussed in section 3.3. In the simulation calculation, a transient was calculated analogously with constant boundary conditions until the steady state was reached. The criteria to stop the transient was a difference below 1% between injected and condensing vapor. In order to achieve the steady state regime faster and thus, to reduce CPU time, modified initial conditions close to those of the permanent regime were defined. Therefore, a modified initial pressure of  $P_{mod} = 3.0 \times 10^5 Pa$  and a modified initial temperature of  $T_{mod} = 389.15 K$  were assumed.

In the experiment, vapor is not present in initial state. The amount of air [mol] that is present in the test facility at initial state is:

$$n_{nc,0} = \frac{P_0 V}{RT_0}$$

With  $P_0$  and  $T_0$  the pressure and the temperature at initial state and  $V$  the volume of MISTRA. In the calculation, the amount of mass present in the modified initial state is:

$$n_{tot,mod} = \frac{P_{mod} V}{RT_{mod}}$$

The mole fraction of air in the modified state conserves the amount of air initially present in the MISTRA facility. The mole fraction of air in the modified initial state is:

$$x_{nc,mod} = \frac{n_{nc,0}}{n_{tot,mod}} = \frac{P_0 \cdot T_{mod}}{T_0 \cdot P_{mod}} = 0.445.$$

The corresponding mass fraction of air is:

$$y_{nc,mod} = \frac{M_{nc} \cdot x_{nc,mod}}{M_{nc} \cdot x_{nc,mod} + M_v (1 - x_{nc,mod})} = 0.563 .$$

In the modified initial state, the gases in the test vessel are considered being at rest and perfectly mixed.

After a transient of about 400 s the steady state is reached. Fig.9 shows the distribution of main quantities in the containment vessel at this instant in a vertical cut-plane. This plane is located at an angle of  $90^\circ$  of the  $180^\circ$  calculation domain (normal to the x-axis). The results of the *fine model* are shown, namely the distribution of the water vapor mass fraction in Fig.9a and of the gas temperature in Fig.9b. The gas velocity in the cavity is shown in Fig.9c. The vectors give the direction of the velocity and the magnitude is shown in color scale.

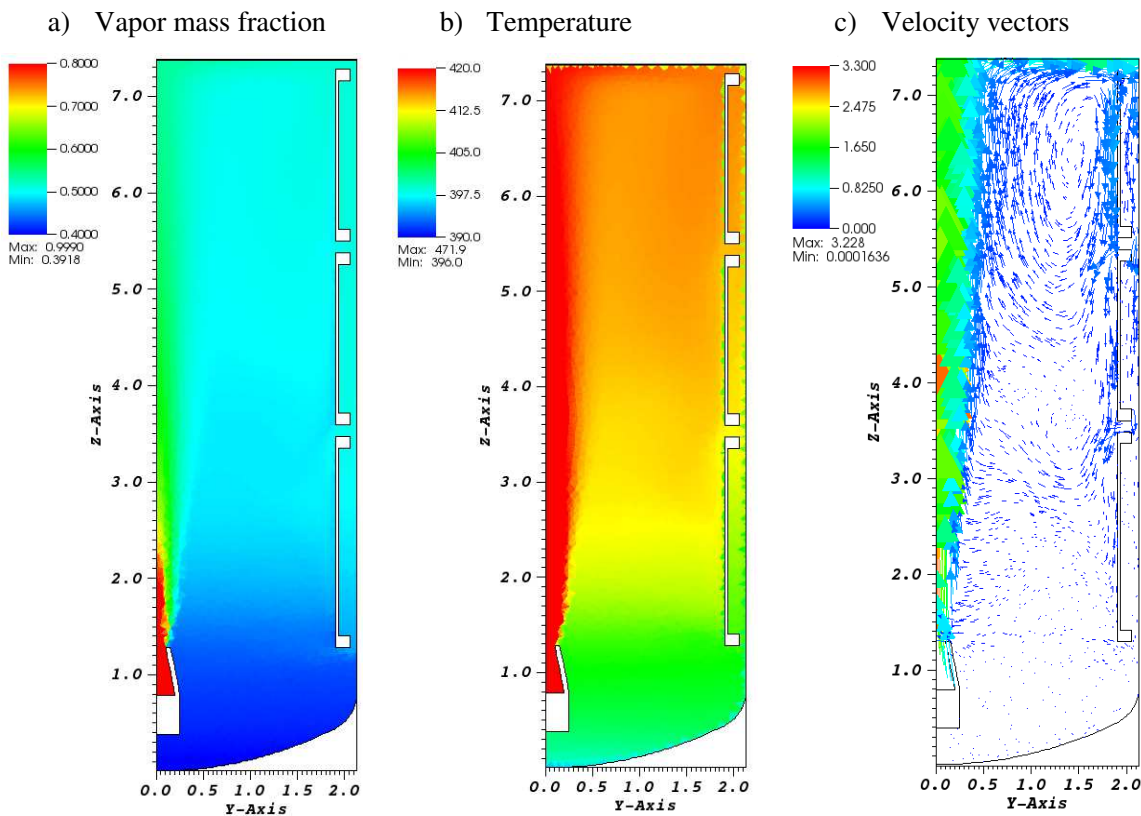


Fig.9 Spatial distribution of main quantities in steady state situation of phase A: a) water vapor mass fraction, b) temperature and c) velocity vectors

The formation of the stratification of the vapor concentration and of the temperature is readily visible. As water vapor condenses on the condenser surfaces, heavier air-rich gas flows to the vessel bottom. This process is intensified by the heat

losses to the condensers, which create cold boundary layers with higher densities. Due to the thermal and species stratification, a zone of stagnant fluid establishes in the vessel bottom. Molecular transport processes control in this zone the heat and mass transfer. In the upper third of the vessel, mixed and forced convection becomes the dominant exchange process, visible by the large convection loop.

Measured and calculated integral quantities at steady state are compared in Table 3. Volume averaged mean values of gas temperature and vapor mass fraction were determined for the calculations. The measured mean temperature and mass fractions correspond to the mean value taken along the vertical profile R2 of Fig.7b. According to Studer et al. (2007), this mean value corresponds to a realistic global mean value. Additionally, the pressure in the facility is compared.

Table 3 Comparison of measured and calculated integral quantities of phase A

	Pressure [Pa]	Vapor mass fraction [-]	Air mass fraction [-]	Temperature [K]
ISP47	329800	0.479	0.521	396.85
<i>Basic model</i>	372100	0.499	0.501	422.35
<i>Improved model</i>	355700	0.488	0.512	412.15
<i>Fine model</i>	346600	0.483	0.517	407.69

In general, the calculations progressively approach the experimental data with improvement of the modelling. In particular, adiabatic external wall lead to significant overestimations of the mean gas temperature. In this case, the heat loss of the external vessel walls to the environment and spurious condensation on this wall is ignored. Since the pressure is a function of temperature, the final pressure is overestimated accordingly. Adding heat losses to the environment and spurious condensation in the *improved model*, all compared quantities improve significantly compared to the *basic model*. Taking further into account finer meshing, heat losses to the environment and spurious condensation, the *fine model* shows a significant better accord to the experiment. This is true for both mean temperature and mean vapor mass fraction. With the *fine model*, the final pressure is estimated with an error of about 5%, but the mean gas temperature is still considerably overestimated. A first ranking of the importance of model improvements show that modelling the heat loss of the external vessel wall to the environment and spurious condensation on this wall is more important for a correct representation of the benchmark than the mesh refinement.

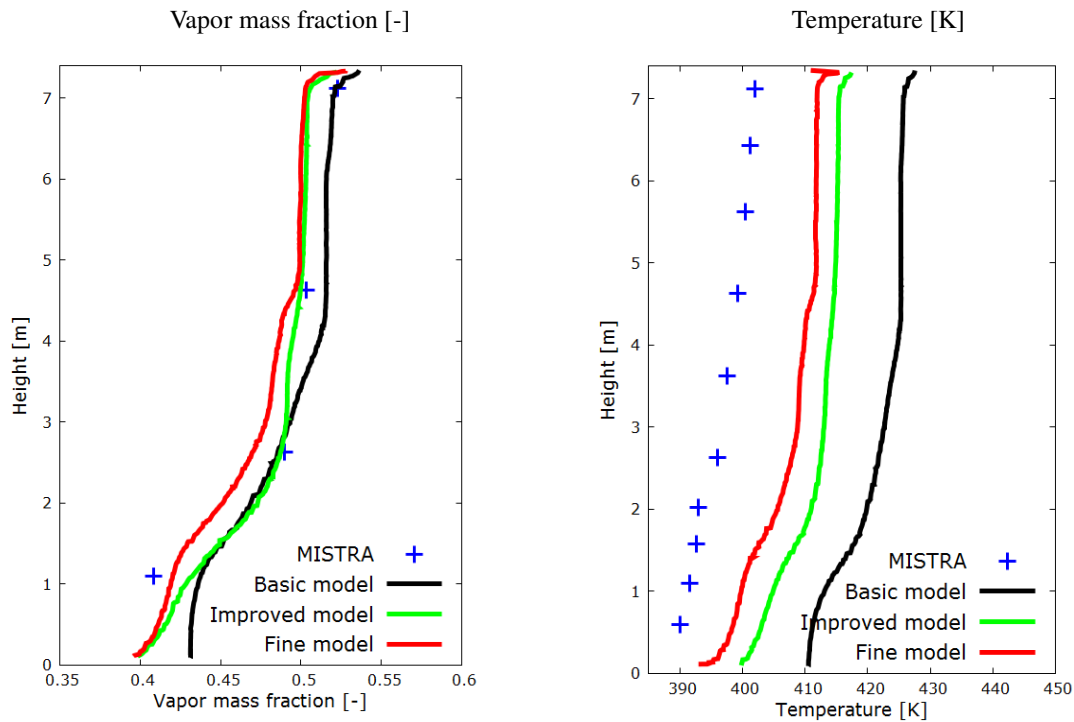


Fig. 10 Comparison of measured and calculated vertical profiles at  $y=0.95$  m (profile R2 in Fig.7b) of the vapor mass fraction (a) and the temperature (b)

In Fig. 10 are compared local vertical profiles of the vapor mass fraction (Fig.10a) and of the temperature (Fig.10b). The profiles are measured at an azimuthal angle of  $345^\circ$  and a distance from the center axis of  $y = 0.95\text{ m}$ . This profile is called R2 in Fig.7b. The profile of the water vapor concentration is only slightly sensitive to the model case. The *fine model* reproduces well the measured stratification near the bottom of the vessel. In contrast, the calculated temperature profiles are very sensitive to the model case. The vertical courses of the temperature profiles are very similar. However, taking the *fine model* profile as reference, an almost constant positive shift of the *improved model* profile by about  $5\text{ K}$  is observed. The *basic model*'s profile is shifted to higher temperatures by approximately  $15\text{ K}$ . This shift of the temperature profile confirms the integral results given in Table 3. In the cases of *improved model* and *fine model* heat losses to the environment and spurious condensation were added by imposing the experimentally derived temperature distribution of the vessel wall. This modification significantly improves the comparison to the experiment. Both temperature and vapor mass fraction decrease and approach the experimental courses. The *fine model*, and here especially the refined mesh on the vessel wall, further improves the comparison. Nevertheless, the impact of refining the mesh is less important than correcting for heat losses and spurious condensation.

Finally, it should be noted that the center velocity of the jet at  $z = 3.6\text{ m}$  is with about  $1.5\text{ m/s}$  in the order of magnitude of ISP47 measurements of 2002 (Studer et al. 2007). Table 4 compares measured and calculated condensation fluxes on the condensers and spurious condensation on the external wall.

Table 4 Condensation mass flow in g/s on condensers and on the external vessel wall

Condenser location	ISP47	<i>Basic Model</i>	<i>Improved Model</i>	<i>Fine Model</i>
Top	47.8	67.3	51.2	47.9
Center	39.3	30.6	29.0	28.7
Bottom	28.7	31.8	21.5	23.2
External wall	15.2	0	27.9	24.7
Total	131.0	129.7	129.7	129.7

Although the total condensation flow is calculated in accordance to the experiment for all models, the calculated distribution of the mass flow on the different condensers and the external wall is not very satisfying. The condensation mass flow on the top condenser is calculated in accordance to the experiment (*improved* and *fine model*). However, the spurious condensation is significantly overestimated. In order to compensate for this overestimation, the condensation mass flow on the center and bottom condensers are underestimated. Nevertheless, the *fine model* represents the condensations flow in acceptable accordance to the experiment. The overall quality of the *fine model* calculation is comparable to the accordance found by the benchmark participants by using specific containment codes (NEA/CSNI, 2007).

#### 4.6 Steady state solution of phase B

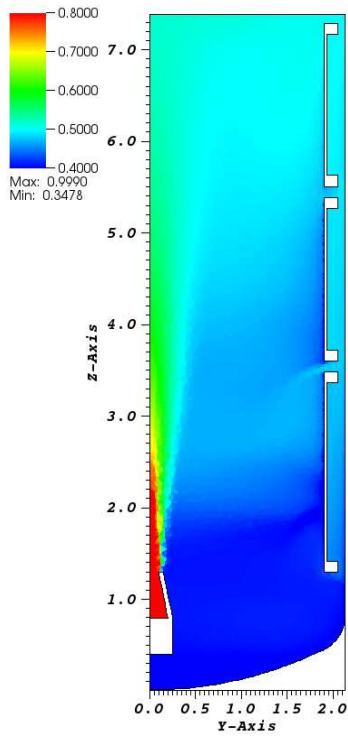
In phase B of the ISP47 transient, water vapor is injected into the MISTRA containment, in which a mixture of two incondensable gases was present, namely air and helium. As for phase A, a transient was calculated with constant boundary conditions until the steady state was reached. The external vessel wall was assumed  $4.5\text{ K}$  warmer than in phase A. In order to achieve the steady state regime faster, modified initial conditions close to those of the permanent regime were defined. The modified initial pressure was set to  $P_{mod} = 5.0 \times 10^5\text{ Pa}$  and the modified initial temperature to  $T_{mod} = 399.15\text{ K}$ . The initial masses of air and helium are given in Table 2. In the modified state, the mass fraction of air, helium and water vapor are  $0.478$ ,  $0.076$  and  $0.446$ , respectively. The gases are considered being at rest and perfectly mixed. The spurious condensation and the vertical distribution of the temperature of the external vessel wall have been estimated from eq.(19). In the absence of a better estimation, the local wall temperature has been increased linearly by  $4.5\text{ K}$ , what corresponds to the difference between the measured mean gas temperatures of phase A and phase B.

After a transient of about  $400\text{ s}$  the steady state is reached. In analogy to phase A, Fig.11 shows for phase B the distribution of main quantities in the containment vessel at steady state in a vertical cut-plane. The results of the *fine model* are shown, namely the distribution of the water vapor mass fraction in Fig.11a, of the helium mass fraction in Fig.11b and of the gas temperature in Fig.11c. The gas velocity in the cavity is shown in Fig.11c; the vectors give the direction of the velocity and the magnitude is shown in color scale.

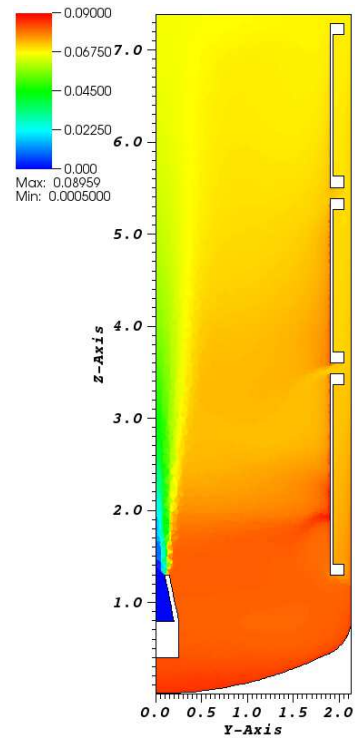
The formation of the stratification of the concentration fields and of the temperature is readily visible. On the one hand, as water vapor condenses on the condenser surfaces and on the vessel wall, heavier gas accumulates near the vessel bottom. On the other hand, air and helium accumulate also in the vessel at a vertical height of the center condenser. Thus, two zones with reduced water vapor concentration establish that are separated by a zone of higher vapor concentration. These zones of

low water vapor concentration are characterized as stagnant fluid with very low velocities (Fig.11d). Molecular transport processes control in these zones the heat and mass transfer.

a) Vapor mass fraction



b) Helium mass fraction



c) Temperature

d) Velocity vectors



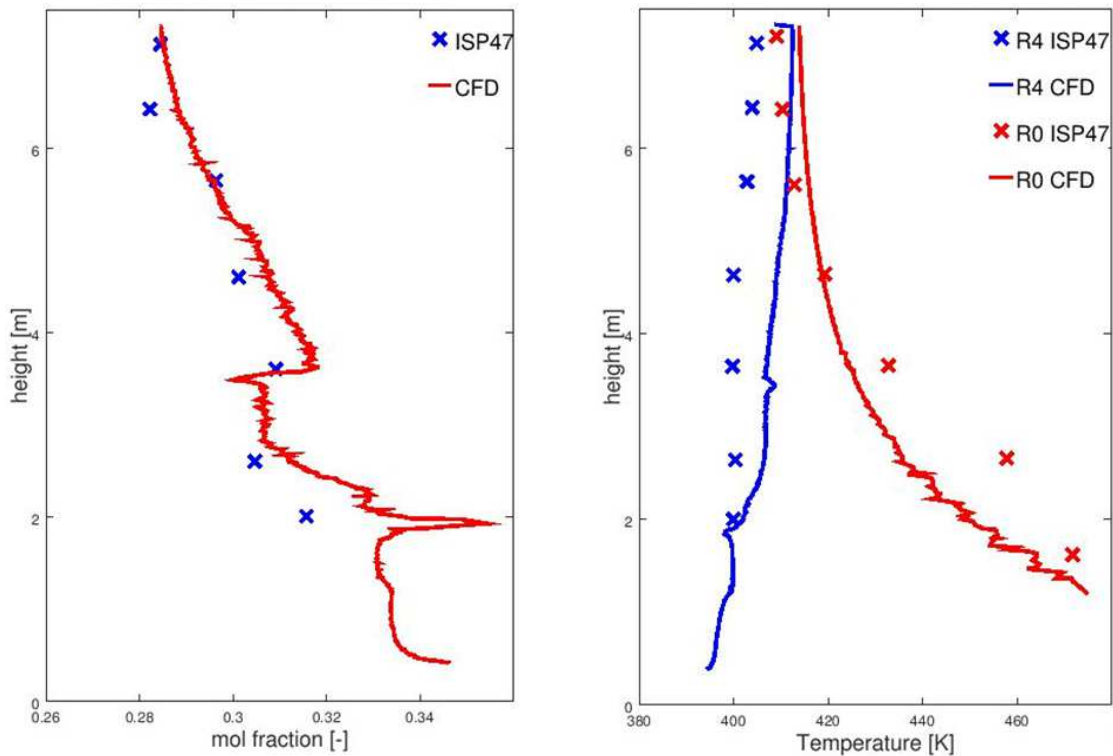


Fig.12 Comparison of measured and calculated vertical profiles: a) the helium mole fraction at  $y=1.815$  m (R4 in Fig.7b) and b) the temperature in the centerline of the vessel and close to the condensers (R0 and R4 in Fig.7b)

The helium concentration profile is measured close to the condensers at the location R4 that is at  $y = 1.815$  m. The temperature profiles are compared for the vessel centerline at  $y = 0$  m (R0) and close to the condensers at R4. This comparison confirms the results given in Table 5. The vertical distribution of helium is very good represented by the calculation. In contrary to this, the temperature close to the condensers is overestimated in the calculation and, close to the injection nozzle outlet, the calculated temperature of the central jet does not follow the measured profile. It seems that the meshing in the central jet is not sufficiently fine. Mesh refinement in the jet region would however reduce the integration time step when using the Euler explicit time scheme. The development of an implicit integration scheme is planned for the future.

Table 6 compares measured and calculated condensation flows on the condensers and spurious condensation on the external wall. It is evident that the spurious condensation is overestimated. Therefore, the condensation mass flow on the condensers is underestimated.

Table 6 Condensation mass flow in g/s on condensers and on the external vessel wall

Condenser location	ISP47	CFD
Top	56.603	45,90
Center	27.0924	21,41
Bottom	29.1711	24,99
External wall	17.900	37,16
Total	130.7665	129,47

Taking into account the overestimation of spurious condensation on the vessel wall, comparison of calculated and measured condensation mass flow on the three condensers is reasonable. The reduced condensation on the center condenser is calculated correctly. The overall quality of the CFD calculation for phase B is comparable to the accordance found by the benchmark participants by using specific containment codes (NEA/CSNI, 2007).

## 5. CONCLUSION

Water vapor condensation on cold walls is an important issue to assure the integrity of the containment in the case of a severe accident in nuclear reactors. A model describing the condensation of water vapor on cold walls was introduced in the *TrioCFD* code. Four verification test cases were analyzed successfully:

- The correct conservation of the species' mass without condensation was tested by a numerical mixing experiment in a closed cavity (comparison to an analytical solution).
- The conservation of the mass of species in the case of condensation was verified for a closed cavity by condensing water vapor on a cold wall (comparison to an analytical solution).
- The correct mass balance was tested for a closed cavity with water vapor injection by predicting an equilibrium of simultaneous vapor injection and condensation.

Then, the MISTRA experiment of the International Standard Problem ISP47 was analyzed, where water vapor is injected into a closed containment vessel under controlled thermal hydraulic conditions. The steady state phases A and B of the experimental procedure were reproduced numerically.

- For phase A, where water vapor and one incondensable gas (air) was present in the MISTRA facility, the results of the calculations approach the experimental values after successive improvement of the modelling. Total pressure and mean mass fractions of air and water vapor were predicted in accordance to the experiment, the gas temperature was overestimated. The measured vertical profile of the water vapor mass fraction was reproduced correctly.
- The steady state of phases B, where water vapor and two incondensable gases (air and helium) were present in the MISTRA facility, was reproduced in accordance to the experiment. Pressure and mean mass fractions were calculated correctly as well as measured vertical profile of the helium mole fraction. As in phase A, the temperature is overestimated.

In general, the CFD calculations reproduce the MISTRA ISP47 experiments in accuracy that is similar to that of the benchmark participants, although the participants have used specific containment codes. In order to improve the results further, it is planned to introduce momentum transport by condensation and heat transfer by species. Further, temperature dependent physical properties will be used as well as a more appropriate equation of state.

Yet importantly, the mesh refinement used for the MISTRA facility calculations with 97 m<sup>3</sup> will lead to about 2.5 milliard tetrahedral cells for simulating the flow in containments of French nuclear reactors, which have an open volume of about 80,000 m<sup>3</sup>. *TrioCFD*, especially when using the performance of GPU processors, treats regularly CFD problems of such size. Hence, it seems possible to date to analyze containment flow of real nuclear containments by CFD by respecting Best Practice Guidelines.

## ACKNOWLEDGEMENT

This work was granted access to the HPC resources of TGCC under the allocation A0072A07571 made by GENCI.

## REFERENCES

- W. Ambrosini, M. Bucci, N. Forgiione, F. Oriolo, S. Paci, J-P. Magnaud, E. Studer, E. Reinecke, S. Kelm, W. Jahn, J. Travis, H. Wilkening, M. Heitsch, I. Kljenak, M. Babić, M. Houkema, D.C. Visser, L. Vyskocil, P. Kostka, R. Huhtanen (2008) Comparison and Analysis of the Condensation Benchmark Results. The 3<sup>rd</sup> European Review Meeting on Severe Accident Research (ERMSAR-2008), Nesseber, Bulgaria, 23-25 September
- P.-E. Angeli, M.-A. Puscas, G. Fauchet and A. Cartalade (2018) FVCA8 Benchmark for the Stokes and Navier–Stokes Equations with the TrioCFD Code—Benchmark Session. In: Finite Volumes for Complex Applications VIII - Methods and Theoretical Aspects, New York: Springer-Verlag, pp.181-202
- P.-E. Angeli, Bieder U., Fauchet G. (2015) Overview of the TrioCFD code: main features, V&V procedures and typical applications to nuclear engineering. *NURETH-16*. Chicago.
- Bieder U., H. Uitslag-Doolaard, B. Mikuz (2021) Investigation of pressure loss and velocity distribution in fuel assemblies with wire-wrapped rods by using RANS and LES with wall functions. *Annals of Nuclear Energy* 152 (2021) 108025
- R.B. Bird, W.E. Steward, E.N. Lightfoot (1960) *Transport Phenomena*. John Wiley & Sons, New York

- Bucci M., M. Sharabi, W. Ambrosini, N. Forgiione, F. Oriolo, S. He (2008) Prediction of transpiration effects on heat and mass transfer by different turbulence models. *Nuclear Engineering and Design* 238, 958–974
- Dehbi A., F. Janasza, B. Bell (2013) Prediction of steam condensation in the presence of noncondensable gases using a CFD-based approach. *Nuclear Engineering and Design* 258 199– 210
- Ducros F., Bieder U., Cioni O., Fortin T., Fournier B., Fauchet G., Quéméré P. (2010) Verification and validation considerations regarding the qualification of numerical schemes for LES for dilution problems. *Nuclear Engineering and Design*, 240, 2123-2130.
- Elmo, M., Cioni, O. (2003) Low Mach number model for compressible flows and application to HTR. *Nuclear Engineering and Design* 222, 117-124.
- FLUENT, 2009. ANSYS FLUENT 12.0/12.1 Documentation.
- Hirt C.V., Nichols B.D., Romero N.C. (1975) SOLA - A numerical solution algorithm for transient flow. Los Alamos National Lab., Report LA-5852.
- Ishay L., Bieder U., Ziskind Z., Rashkovan A. (2015) Turbulent jet erosion of a stably stratified gas layer in a nuclear reactor test containment. *Nuclear Engineering and Design*, 292, 133–148.
- Kader B. (1991) Heat and Mass transfer in Pressure-Gradient boundary layers. *Int. Jour. of Heat and Mass Transfer*, 34, 2837-2857
- Kassem S. (2020) Assessment of TrioCFD to treat vapor condensation on cold containment walls. Master Thesis, University of Pisa, etd-01272020-144126
- Kelm S., M. Kampili, G. Vijaya Kumar, K. Sakamoto, X. Liu, C. Druska, A. Kuhr, K. Arul Prakash and H.-J. Allelein (2019) Development and First Validation of the Tailored CFD Solver ‘containmentFOAM’ for Analysis of Containment Atmosphere Mixing. NURETH-18, Portland, OR, August 18-22
- Kelm S., Kampili M., Liu X., George A., Schumacher D., Druska C., Struth S., Kuhr A., Ramacher L., Allelein H.-J., et al. (2021) The Tailored CFD Package ‘containmentFOAM’ for Analysis of Containment Atmosphere Mixing, H<sub>2</sub>/CO Mitigation and Aerosol Transport. *Fluids* 6, 100.
- Kim J., R-J Park, G-H Kim (2018) Methodology for Evaluation of hydrogen Safety in a NPP Containment. Transactions of the Korean Nuclear Society Spring Meeting Jeju, Korea, May 17-18
- NEA CSNI (2000) CSNI International Standard Problems (ISP), Brief descriptions (1975-1999). Paris.
- NEA CSNI (2007) International Standard problem ISP-47 on Containment Thermalhydraulics, Final Report. NEA/CSNI/R(2007)10
- Patankar S.V. (1980) *Numerical Heat Transfer and Fluid Flow*. Hemisphere, Washington, DC
- Povilaitis M., E. Urbonavicius, S. Rimkevicius (2014) Validation of special nodalisation features for lumped-parameter injection modelling based on MISTRA facility tests from ISP-47 and SARNET. *Nuclear Engineering and Design* 278, 86–96
- Punetha M., S. Khandear (2017) A CFD based modelling approach for predicting steam condensation in the presence of non-condensable gases. *Nuclear Engineering and Design* 324, 280–296
- Reichardt M. (1951) Vollständige Darstellung der turbulenten Geschwindigkeitsverteilung in glatten Leitungen. *Zeitschrift für Angewandte Mathematik und Mechanik*, Vol 31, p 208
- Saikali E., G. Bernard-Michel, A. Sergent, C. Tenaud, R. Salem (2019) Highly resolved large eddy simulations of a binary mixture flow in a cavity with two vents: Influence of the computational domain. *Int. Journal of hydrogen energy*, 44, 8856-8873
- Studer E., Magnaud, J.-P., Dabbene, F. and Tkatschenko, I. (2007) International standard problem on containment thermal-hydraulics ISP47 Step 1 - Results from the MISTRA exercise. *Nuclear Engineering and Design* 237, 536-551.
- Studer, E., Brinster, J., Tkatschenko, I., Mignot, G., Paladino, D., Andreani, M., (2012) Interaction of a light gas stratified layer with an air jet coming from below: largescale experiments and scaling issues. *Nuclear Engineering and Design* 253, 406–412.

Studer E., D. Abdo, S. Benteboula, G. Bernard-Michel, B. Cariteau, N. Coulon, F. Dabbene, Ph. Debesse, S. Koudriakov, C. Ledier, J.-P. Magnaud, O. Norvez, J.-L. Widloecher, A. Beccantini, S. Gounand, J. Brinster (2019) Challenges in Containment Thermal hydraulics. NURETH-18, Portland, OR, August 18-22

Studer E. (2019). Privat communication.

Tkatschenko, I., Studer, E. and Paillère, H. (2005) MISTRA Facility for Containment Lumped Parameter and CFD Codes Validation: Example of the International Standard Problem ISP47. Nuclear Energy for New Europe 2005. Bled, Slovenia.

Yadav M.K., Khandekar S. and Sharma P.K. (2016) An integrated approach to steam condensation studies inside reactor containments: A review. Nuclear Engineering and Design 300, 181–20

## NOMENCLATURE

### *Capital letters*

D	Diffusivity	$m^2/s$
M	molar mass	mol/kg
N	number of mols	-
P	pressure	Pa
R	ideal gas constant	$J/(K \cdot mol)$ .
S	surface	$m^2$
T	temperature	K
V	volume	$m^3$
$\vec{V}$	velocity vector	m/s
VEF	finite element based finite volume method	
VDF	finite volume method	

### *Small letters*

$c_p$	heat capacity at constant pressure	$J/(kgK)$
d	distance	m
e	internal energy	
f	mole flow	mol/s
g	gravitational acceleration	$m/s^2$
h	enthalpy	
$\dot{m}$	mass flux density	$kg/(m^2s)$
n	amount of a specie	mol
t	time	s
u	velocity	m/s
x, y, z	coordinate direction	-
y	mass fraction	-

### *Greek letters*

$\Delta$	difference	-
$\delta$	Kronecker delta	-
$\lambda$	thermal conductivity	$W/(m \cdot K)$
$\rho$	density	$kg/m^3$
$\mu$	dynamic viscosity	$kg/(m \ s)$ ,

### *Indices*

T	turbulent
b	in the bulk
bo	boundary
c	cold
co	condensation
hy	hydraulic
h	hot
i	at the gas-liquid interface
i, j	indices for Einstein notation
i, j, k	cell number and boundary number
i, j, k	coordinates
k	incondensable gas k
mod	modified
n	instant
nc	incondensable
sat	at saturation
ss	steady state
0	initial state

## ANNEXE I: CONSERVATION OF MOMENTUM

The conservation of momentum can be written in conservative form, where the terms on the right hand side are not added for simplicity:

$$\frac{\partial \rho u_i}{\partial t} + \frac{\partial (\rho u_i u_j)}{\partial x_j} = \dots \quad \text{or} \quad \text{A1-1}$$

$$\rho \frac{\partial u_i}{\partial t} + u_i \frac{\partial \rho}{\partial t} + \rho u_j \frac{\partial u_i}{\partial x_j} + u_i \frac{\partial (\rho u_j)}{\partial x_j} = \dots, \text{ respectively.} \quad \text{A1-2}$$

When applying the conservation equation of the mass:

$$\frac{\partial \rho}{\partial t} + \frac{\partial}{\partial x_j} (\rho u_j) = -\dot{m}_v|_{wall}, \quad \text{A1-3}$$

the conservation equation of momentum reads:

$$\rho \frac{\partial u_i}{\partial t} + \rho u_j \frac{\partial u_i}{\partial x_j} = \dots + u_i m_v|_w \quad \text{A1-4}$$

## ANNEXE II: CONSERVATION OF ENERGY

The balance of internal energy is written without kinetic energy, potentielle energy, radiation and viscose heating. Internal sources (latent heat due to fog formation) and external sources (latent heat due to wall condensation) are not added here for simplicity. The exponents  $\lambda$  and D and stand for heat transport (q) along temperature gradients and heat transport along gradients of species concentration, respectively.

$$\frac{\partial \rho e}{\partial t} + \frac{\partial}{\partial x_j} (\rho u_j e) = \frac{\partial q_j^\lambda}{\partial x_j} + \frac{\partial q_j^D}{\partial x_j} \quad \text{A2-1}$$

Written in enthalpy  $h = e + \frac{P^{th}}{\rho}$  with  $P^{th}$  the thermodynamic pressure the eq.(A2-1) reads:

$$\frac{\partial}{\partial t} \rho \left( h - \frac{P^{th}}{\rho} \right) + \frac{\partial}{\partial x_j} \left( \rho u_j \left( h - \frac{P^{th}}{\rho} \right) \right) = \frac{\partial q_j^\lambda}{\partial x_j} + \frac{\partial q_j^D}{\partial x_j} \quad \text{or} \quad \text{A2-2}$$

$$\frac{\partial \rho h}{\partial t} + \frac{\partial}{\partial x_j} (\rho u_j h) = \frac{\partial q_j^\lambda}{\partial x_j} + \frac{\partial q_j^D}{\partial x_j} + \frac{\partial P^{th}}{\partial t} + \frac{\partial}{\partial x_j} \left( \rho u_j \frac{P^{th}}{\rho} \right) \quad \text{A2-3}$$

With the equation of mass conservation  $\frac{\partial \rho}{\partial t} + \frac{\partial}{\partial x_j} (\rho u_j) = -\dot{m}_v|_{wall}$  and  $P^{th} = \text{constant in space}$ :

$$\rho \frac{\partial h}{\partial t} + \rho \frac{\partial}{\partial x_j} (u_j h) = \frac{\partial q_j^\lambda}{\partial x_j} + \frac{\partial q_j^D}{\partial x_j} + \frac{\partial P^{th}}{\partial t} + h_v \dot{m}_v|_{wall}. \quad \text{A2-4}$$

With  $h = c_p T$  and  $q_j^\lambda = -\lambda \frac{\partial T}{\partial x_j}$  as well as  $q_j^D = -\sum_{k=1}^N \rho D_k h_k \frac{\partial w_j}{\partial x_j}$ , the final energy conservation equation yields:

$$\rho c_p \frac{\partial T}{\partial t} + \rho c_p u_j \frac{\partial T}{\partial x_j} = -\frac{\partial}{\partial x_j} \left( \lambda \frac{\partial T}{\partial x_j} \right) - \sum_{k=1}^N \rho D_k h_k \frac{\partial w_j}{\partial x_j} + c_{p,v} T \dot{m}_v|_{wall} + \frac{\partial P^{th}}{\partial t} \quad \text{A2-5}$$

### ANNEX III: CONSERVATION OF SPECIES

The equation of global mass conservation is written:

$$\frac{\partial \rho}{\partial t} + \frac{\partial}{\partial x_j} (\rho u_j) = -\dot{m}_v|_{wall} \quad A3-1$$

Without taking into account diffusive fluxes, the mass conservation equation for vapor (index v) and the incondensable gas k (index nc,k) are written:

$$\frac{\partial \rho_v}{\partial t} + \frac{\partial}{\partial x_j} (\rho_v u_j) = -\dot{m}_v|_{wall} \quad A3-2$$

$$\frac{\partial \rho_{nc,k}}{\partial t} + \frac{\partial}{\partial x_j} (\rho_{nc,k} u_j) = 0 \quad A3-3$$

The mass fractions  $y_v$ ,  $y_{nc,k}$  and the conservation of species  $y_v + \sum_{k=1}^N y_{nc,k} = 0$  are introduced. Then, the partial derivative of  $\rho_v$  is:

$$\frac{\partial \rho_v}{\partial t} = \frac{\partial(\rho y_v)}{\partial t} = y_v \frac{\partial \rho}{\partial t} + \rho \frac{\partial y_v}{\partial t} \quad A3-4$$

On the one hand, the conservation of vapor can be rewritten:

$$\frac{\partial \rho_v}{\partial t} = y_v \left[ -\dot{m}_v|_{wall} - \frac{\partial}{\partial x_j} (\rho u_j) \right] + \rho \frac{\partial y_v}{\partial t} \quad A3-5$$

$$\frac{\partial \rho_v}{\partial t} = -y_v \dot{m}_v|_{wall} - y_v \frac{\partial}{\partial x_j} (\rho u_j) + \rho \frac{\partial y_v}{\partial t} \quad A3-6$$

On the other hand, the mass conservation of vapor can be written :

$$\frac{\partial \rho_v}{\partial t} = -\dot{m}_v|_{wall} - \frac{\partial}{\partial x_j} (\rho_v u_j) = -\dot{m}_v|_{wall} - \frac{\partial}{\partial x_j} (\rho y_v u_j) \quad A3-7$$

and

$$\frac{\partial \rho_v}{\partial t} = -\dot{m}_v|_{wall} - y_v \frac{\partial}{\partial x_j} (\rho u_j) - \rho u_j \frac{\partial y_v}{\partial x_j} \quad A3-8$$

Equalizing equations. A3-6 and A3-7 leads to:

$$-y_v \dot{m}_v|_{wall} + \rho \frac{\partial y_v}{\partial t} = -\dot{m}_v|_{wall} - \rho u_j \frac{\partial y_v}{\partial x_j} \quad A3-9$$

$$\rho \frac{\partial y_v}{\partial t} + \rho u_j \frac{\partial y_v}{\partial x_j} = \dot{m}_v|_{wall} (y_v - 1) \quad A3-10$$

Analogously can be derived the conservation equation for the incondensable gas k:

$$\rho \frac{\partial y_{nc,k}}{\partial t} + \rho u_j \frac{\partial y_{nc,k}}{\partial x_j} = \dot{m}_v|_{wall} y_{nc,k} \quad A3-11$$